# 2.5D Reverse time migration

Francisco A. da Silva Neto[1,3], Jessé C. Costa[1,3], Jörg Schleicher[2,3], and Amélia Novais[2,3]

[1] Faculty of Geophysics, UFPA, [2] Dept. of Applied Mathematics, IMECC/UNICAMP, [3] INCT-GP

## Abstract

**Reverse time migration (RTM) in 2.5D offers an alternative to improve resolution and amplitude when imaging 2D seismic data. Wave propagation in 2.5D assumes translational invariance of the velocity model. Under this assumption, we implement a finite-difference (FD) modeling algorithm in the mixed time-space/wavenumber domain to simulate the velocity and pressure fields for acoustic wave propagation and apply it in RTM. The 2.5D FD algorithm is truly parallel, allowing an efficient implementation in clusters. Storage and computing time requirements are strongly reduced compared to a full 3D FD simulation of the wave propagation. This feature makes 2.5D RTM much more efficient than 3D RTM, while achieving improved modeling of 3D geometrical spreading and phase properties of the seismic waveform in comparison to 2D RTM. Together with an imaging condition that compensates for uneven illumination and/or the obliquity factor, this allows to recover amplitudes proportional to the earth's reflectivity. Numerical experiments using synthetic data demonstrate the better resolution and improved amplitude recovery of 2.5D RTM relative to 2D RTM.**

## Introduction

The difficulties of imaging steeply dipping reflectors and complex structures in complicated velocity models, for example below salt bodies, has created the need for a migration method that models wave propagation in such media accurately. Reverse-time migration is the best known method capable of handling this challenge.

Additionally to its superior imaging capabilities, advances have been made in amplitude preservation in RTM. Several attempts to improve the amplitudes in RTM are based on illumination compensation with different kinds of stabilization (Valenciano and Biondi, 2003; Kaelin and Guitton, 2006). Attempting to better understand the amplitudes in RTM, Haney et al. (2005) performed an asymptotic analysis of the cross-correlation imaging condition. Their analysis assumes a single planar reflector in a 3D homogeneous medium, full coverage, and infinite aperture. They demonstrate that the amplitudes of RTM are affected by an obliquity factor that depends on the reflector dip. Most recently, Chattopadhyay and McMechan

(2008) explicitly compared the imaging conditions most commonly used in practice to make clear which are viable for recovering accurate amplitudes and which are not. Other useful imaging conditions were recently discussed by Schleicher et al. (2008), Poole et al. (2010), and Liu et al. (2011).

Based on the result of Haney et al. (2005), Costa et al. (2009) proposed a new imaging condition for amplitude preservation in RTM. The idea is to asymptotically correct for obliquity factor by introducing a weight factor in the source-normalized imaging condition. They also report an improvement of the images when the obliquity factor is included together with illumination compensation in the imaging condition for RTM.

The computational demand for 3D pre-stack reverse time migration (RTM) is high compared to wave equation migration by downward extrapolation of the wavefield (Biondi, 2006). Therefore, most practical 3D RTM examples still rely on coarse grids to reduce the computational cost. Nevertheless, low cost parallel computing and more efficient storage hardware is starting to make RTM feasible, particularly in 2D.

However, there is a problem with amplitude recovery in RTM for the case of seismic data acquired on a single line. In this situation, application of RTM generally relies on 2D wave extrapolation techniques. This will harm the efforts to extract meaningful amplitudes since the geometrical-spreading effects of 3D wave propagation are incorrectly simulated. A possible solution to this problem is to extend the model to three dimensions under the assumption of translation invariance and then simulate the wave propagation using 3D techniques. For many applications, however, this procedure is unacceptably expensive, particularly for its storage requirements. A cheaper solution is the use of 2.5D techniques, which explore the medium symmetry to simulate full 3D wave propagation. While 2.5D descriptions of wave propagation are straightforward for ray-based solutions (Bleistein, 1986), such modifications for the finite-difference (FD) method have not been available until recently (Novais and Santos, 2005; Costa et al., 2005). As shown in their works, 2.5D FD simulates wave propagation with the same quality as 3D FD with a reduced computational cost and storage requirements corresponding to 2D FD. Moreover, 2.5D FD is an embarrassingly parallel process that can be efficiently implemented on clusters.

In this work, we demonstrate the application of 2.5D FD methods in RTM. The same conclusions regarding computational cost and storage requirements also apply to 2.5D RTM. Numerical experiments demonstrate the superior quality of 2.5D RTM images as compared to their 2D counterparts, with respect to both, amplitudes and

resolution. As a consequence, 2.5D RTM might even be of interest to produce high-resolution images of selected lines of a 3D survey on a denser grid than can be used for a full 3D RTM.

**Methodology**

As any 2.5D technique, 2.5D RTM assumes the medium to be translation invariant in the direction perpendicular to the seismic line. It relies on 2.5D FD, which explores this symmetry of the velocity model to simplify the simulation of full 3D wave propagation. Below, we give a brief introduction to the 2.5D FD method.

*2.5D finite differences*

Using index notation and summation convention, the system of equations that governs the acoustic wavefield in 3D is

$$\rho(\mathbf{x})\frac{\partial v_j(\mathbf{x},t)}{\partial t} = -\frac{\partial p(\mathbf{x},t)}{\partial x_j} + f_j(\mathbf{x},t);$$
$$\frac{\partial p(\mathbf{x},t)}{\partial t} = -\rho(\mathbf{x})c^2(\mathbf{x})\frac{\partial v_j(\mathbf{x},t)}{\partial x_j} + \frac{\partial q(\mathbf{x},t)}{\partial t}; \quad (j=1,2,3); \quad (1)$$

where $\rho$ is the medium mass density, $c$ is the propagation velocity, $v_j$ and $p$ are the velocity and pressure wavefields, $f_j$ represents a dipole source and $q$ the rate of injection of an explosive source.

Let the direction of translational invariance of the medium be denoted by the $x_2$ coordinate. Because the medium properties are independent of $x_2$, it is then convenient to apply a Fourier transform in that direction to the acoustic wavefield, viz.,

$$v_j(\mathbf{x},t) = \int_{-\infty}^{\infty} V_j(\mathbf{X},k_2,t)\exp(ik_2x_2)\,dk_2 , \quad (2)$$

and

$$p(\mathbf{x},t) = \int_{-\infty}^{\infty} P(\mathbf{X},k_2,t)\exp(ik_2x_2)\,dk_2 , \quad (3)$$

where $k_2$ is the wavenumber associated with $x_2$ and $\mathbf{X} \equiv (x_1,x_3)$. Moreover, $V_j(\mathbf{X},k_2,t)$ and $P(\mathbf{X},k_2,t)$ denote the complex valued components of the acoustic wavefield in the mixed $(\mathbf{X},k_2,t)$-domain. The source distributions $q$ and $f_j$ can be represented in a similar way in using their counterparts $Q$ and $F_j$, respectively, in this domain.

The components of the acoustic wavefield and its source distributions are solution of the complex-valued system

$$\rho(\mathbf{X})\frac{\partial V_J}{\partial t} = -\frac{\partial P}{\partial X_J} + F_J$$
$$\rho(\mathbf{X})\frac{\partial V_2}{\partial t} = -ik_2P + F_2$$
$$\frac{\partial P}{\partial t} = -\rho(\mathbf{X})c^2(\mathbf{X})\left(\frac{\partial V_J}{\partial X_J} + ik_2V_2\right) + \frac{\partial Q}{\partial t} \quad (4)$$

where the index $J$ assumes only the values 1 and 3.

We assume the source distributions have specular symmetry with respect to the $x_1$-$x_3$ plane. This is true, e.g., for a explosive source or any other source the forces or moments of which are either located entirely within the $x_1$-$x_3$ plane or have equal out-of-plane components in the positive and negative $x_2$ direction. This symmetry implies:

1- the dipole source component in the $x_2$ direction vanishes, i.e., $f_2 = 0$;

2- the velocity components $v_J(\mathbf{x},t)$ are even functions of $x_2$ and, thus, their Fourier transforms $V_J(\mathbf{X},k_2,t)$ are real-valued quantities;

3- the velocity component $v_2(\mathbf{x},t)$ is an odd function of $x_2$ and, thus, its Fourier transform $V_2(\mathbf{X},k_2,t)$ is a purely imaginary quantity.

Defining $U_2(\mathbf{X},k_2,t) \equiv iV_2(\mathbf{X},k_2,t)$, the acoustic wavefield in the mixed space/wavenumber domain satisfies the real-valued system

$$\rho(\mathbf{X})\frac{\partial V_J}{\partial t} = -\frac{\partial P}{\partial X_J} + F_J ,$$
$$\rho(\mathbf{X})\frac{\partial U_2}{\partial t} = k_2P ,$$
$$\frac{\partial P}{\partial t} = -\rho(\mathbf{X})c^2(\mathbf{X})\left(\frac{\partial V_J}{\partial X_J} + k_2U_2\right) + \frac{\partial Q}{\partial t} . \quad (5)$$

The numerical solution of this system of equations by finite differences is discussed in Costa et al. (2005). After solving this system of equations, the acoustic wavefield in the space-time domain can be computed from

$$v_J(x_1,x_2,x_3,t) = \frac{1}{2\pi}\int_{-\infty}^{+\infty} V_J(x_1,k_2,x_3,t)e^{ik_2x_2}\,dk_2, \quad (6)$$

$$v_2(x_1,x_2,x_3,t) = -\frac{i}{2\pi}\int_{-\infty}^{+\infty} U_2(x_1,k_2,x_3,t)e^{ik_2x_2}\,dk_2, \quad (7)$$

and

$$p(x_1,x_2,x_3,t) = \frac{1}{2\pi}\int_{-\infty}^{+\infty} P(x_1,k_2,x_3,t)e^{ik_2x_2}\,dk_2 . \quad (8)$$

The algorithm represented by this set of equations requires the solution of an independent 2D FD system of equations in the $(\mathbf{X},t)$-domain for each wavenumber $k_2$. This can be implemented very efficiently in a parallel architecture with each value of $k_2$ being assigned to a different processing unit.

We use this algorithm to implement RTM in 2.5D. For each common-shot gather the source wavefield is propagated forward in time. Afterwards, the receiver wavefield is backpropagated in time and the imaging condition is applied at every time step. The final migrated image is the stack of all common shot images.

*2.5D reverse time migration*

The cross-correlation imaging condition for shot-profile migration reads (Claerbout, 1985)

$$I(\mathbf{x}) = \sum_{\mathbf{x}_s}\sum_{\mathbf{x}_g}\int_0^{t_{max}} p_s(\mathbf{x},t;\mathbf{x}_s)\,p_g(\mathbf{x},t;\mathbf{x}_g)dt . \quad (9)$$

It produces an image, $I(\mathbf{x})$, by cross-correlating two wavefields with zero temporal and spatial lag. The two wavefields are $p_s(\mathbf{x},t;\mathbf{x}_s)$, which represents the forward propagated wavefield from the source, $\mathbf{x}_s$, to the image point, $\mathbf{x}$, and $p_g(\mathbf{x},t;\mathbf{x}_g)$, which represents the receiver wavefield that is backpropagated in reverse time from the receiver, $\mathbf{x}_g$, to the image point. Here, $t_{max}$ is maximum recorded time.

The cross-correlation imaging condition (equation 9) does not take into account other issues that may affect the resulting amplitude when applying RTM in complex velocity models, like the lack of full coverage of sources and receivers and the uneven illumination of the targets. Illumination compensation is achieved by normalizing the cross-correlation imaging condition by the source energy at the imaging point (Biondi, 2006)

$$I(\mathbf{x}) = \int_{\mathbf{x}_s} \frac{\int_{\mathbf{x}_g} \int_0^{t_{max}} p_s(\mathbf{x},t;\mathbf{x}_s)\,p_g(\mathbf{x},t;\mathbf{x}_g)\,dt\,d\mathbf{x}_g}{\int_0^{t_{max}} p_s(\mathbf{x},t;\mathbf{x}_s)\,p_s(\mathbf{x},t;\mathbf{x}_s)\,dt}\,d\mathbf{x}_s\,. \qquad (10)$$

Note that the illumination compensation in equation 10 is calculated from in-plane propagation but is actually needed to compensate for out-of-plane geometric-spreading loss. In complex settings, this might lead to nonoptimal amplitude treatment.

However, illumination compensation (equation 10) is known to enhance migration artifacts. An improved imaging condition combines the illumination compensation with an obliquity factor weight function in the imaging condition (Costa et al., 2009)

$$I(\mathbf{x}) = \int_{\mathbf{x}_s} \frac{\int_{\mathbf{x}_g} \int_0^{t_{max}} W(\mathbf{S}_s,\mathbf{S}_g)\,p_s(\mathbf{x},t;\mathbf{x}_s)\,p_g(\mathbf{x},t;\mathbf{x}_g)\,dt\,d\mathbf{x}_g}{\int_0^{t_{max}} p_s(\mathbf{x},t;\mathbf{x}_s)\,p_s(\mathbf{x},t;\mathbf{x}_s)\,dt}\,d\mathbf{x}_s\,, \qquad (11)$$

where $\mathbf{S}_s$ represents the Poynting vector of the source wavefield and $\mathbf{S}_g$ represents the Poynting vector of the receiver wavefield. These Poynting vectors are calculated from

$$\mathbf{S}_\alpha = \mathbf{v}_\alpha p_\alpha \qquad (\alpha = s,g)\,, \qquad (12)$$

where $\mathbf{v}_\alpha$ and $p_\alpha$ are the velocity and pressure wavefields as defined above. The weight function consists of two independent factors

$$W(\mathbf{S}_s,\mathbf{S}_g) = \cos^3\alpha \cos^3\theta\,, \qquad (13)$$

where $\cos^3\alpha$ is the obliquity compensation factor and $\cos^3\theta$ is a scattering angle taper. Both factors can be applied individually or jointly. The scattering angle taper is a modification of the original idea of Yoon and Marfurt (2006) to allow only for certain scattering angles in the imaging condition.

Both the scattering angle $\theta$ and the propagation angle $\alpha$ can be determined from directional information of the Poynting vectors. Let us denote the normalized Poynting vectors by

$$\widehat{\mathbf{S}}_\alpha = \frac{\mathbf{S}_\alpha}{\|\mathbf{S}_\alpha\|} \qquad (\alpha = s,g)\,. \qquad (14)$$

Then, the scattering angle $\theta$ is given by

$$\cos^2\theta = \frac{1}{2}\left(1 + \widehat{\mathbf{S}}_s \cdot \widehat{\mathbf{S}}_g\right)\,, \qquad (15)$$

and the propagation angle $\alpha$, i.e., the angle between the bisection of the propagation directions and the vertical, by

$$\cos\alpha = \begin{pmatrix} 0 \\ 0 \\ 1 \end{pmatrix} \cdot \left(\frac{\widehat{\mathbf{S}}_s + \widehat{\mathbf{S}}_g}{\|\widehat{\mathbf{S}}_s + \widehat{\mathbf{S}}_g\|}\right)\,. \qquad (16)$$

When applied together with the 2.5D simulation of 3D wave propagation, the weighted imaging condition in equation 11 will help to improve the amplitude recovery from the migration of 2D seismic data using RTM.
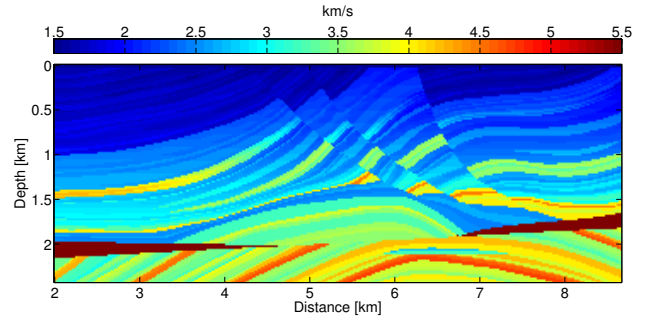


Figure 1: Marmousi velocity model. The dark red high-velocity zones in the lower part of the model represent salt intrusions.
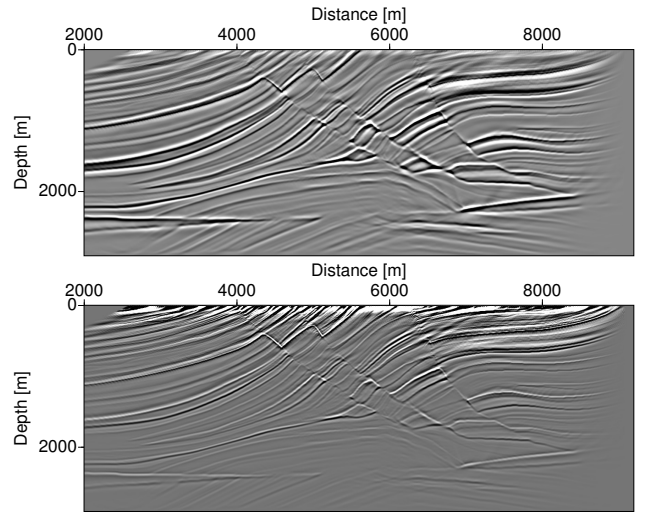


Figure 2: RTM images computed using the cross-correlation imaging condition (equation 9). Top: 2D image; bottom: 2.5D image.

**Numerical experiments**

We evaluate the 2.5D RTM technique discussed above using the Marmousoft synthetic data set (Billette et al., 2003). This data set was simulated using the ray-Born approximation in 2.5D. The velocity model for raytracing is a smoothed version of the original Marmousi velocity model (see Figure 1). The absence of multiples and the correct computation of 3D geometrical spreading makes this synthetic data set the ideal benchmark for the first test of our 2.5D RTM algorithm. The data set consists of 261 common-shot gathers with 96 receivers per shot, regularly spaced at 25 m. The nearest offset is 100 m. The recording time is 3 s with a 4 ms sampling interval.

The velocity model is defined on a regular mesh with 485 nodes in the vertical direction and 1533 nodes in the horizontal direction. Node spacing is 6 m. The source wavefield was simulated using a Blackman-Harris wavelet (Harris, 1978; Chen et al., 1997) with a peak frequency of 30 Hz.
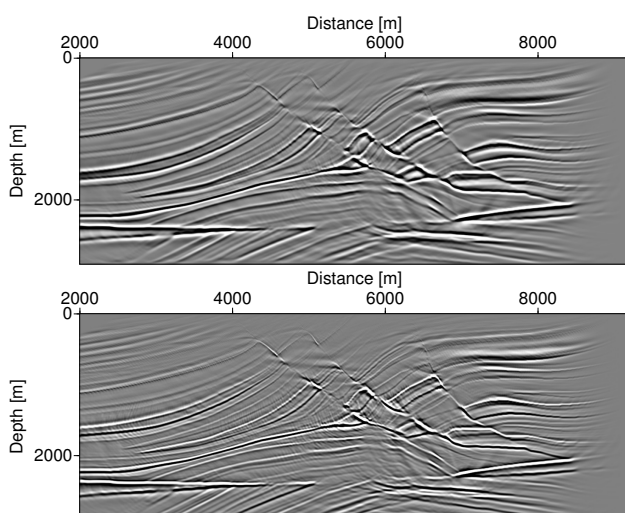
Figure 3: RTM images computed with illumination compensation imaging condition (equation 10). Top: 2D image; bottom: 2.5D image.
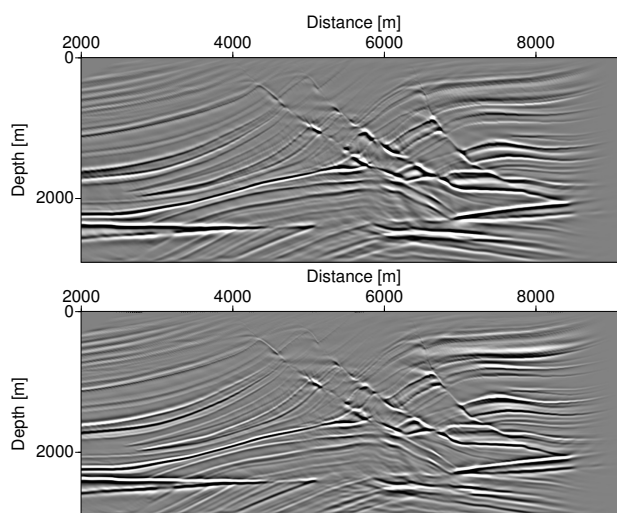


Figure 4: RTM images computed with scattering angle taper as a weight function in the weighted imaging condition (equation 11). Top: 2D image; bottom: 2.5D image.

*Experiment with conventional imaging condition*

Figure 2 compares the results of 2D and 2.5D RTM using the cross-correlation imaging condition of equation 9. Note that we have not applied any post-processing filters like a Laplacion to this or any of the following images. The most eye-popping difference between these images is their amplitude behavior. The events in the 2D migrated image have a much smaller amplitude variation from top to bottom when compared to the 2.5D migrated image. This feature reflects the difference in the geometrical-spreading factor between the 2D and 3D propagation. The geometrical spreading for 2D propagation is much smaller than that for 3D. Moreover, closer inspection reveals different pulse shapes and an improvement in resolution.

While the 2D amplitude behavior actually might be desirable, there is another remarkable difference between the 2D and 2.5D images with respect to resolution. It is evident from Figure 2 that the 2.5D migrated image has a better resolution than the 2D image. Note that the events in the central part of the model, the limits of the faults, and the thin layers are much better defined. A more detailed analysis also reveals a phase difference between the pulses, namely a symmetric pulse for the 2.5D RTM and a nonsymmetric pulse for 2D RTM. The reason for both the differences in resolution and phase is that 3D propagation simulates a point source while 2D propagation simulates a line source. Line sources add a phase rotation and a half-derivative to the source pulse, while point sources add a full derivative and no phase rotation. Thus 2.5D RTM preserves a higher frequency content of the wavelet.

*Experiment with illumination compensation*

The amplitude decay in the 2.5D image of Figure 2 can be compensated for by illumination correction. The second numerical experiment uses the imaging condition with amplitude compensation (equation 10). Figure 3 shows the results of 2D and 2.5D RTM, respectively.

The illumination compensation resulted in a good equalization of the amplitudes in both images for most of the events and eliminated the strong amplitude differences between the images. However, more subtle amplitude differences are still noticeable, particularly in the lower left portion of the images below 2000 m. The 2.5D RTM image presents larger differences between the amplitudes of different reflectors. This behavior is in agreement with the reflectivity in this area. The strongest impedance contrast, i.e., that between the sediments and the salt intrusions (see again Figure 1) has the highest amplitudes. Moreover, the illumination compensation strongly highlights the difference in resolution and phase between 2.5D and 2D RTM. This is clearly visible in the whole images, but particularly in the region between 5000 m-8000 m and at the bottom-of-salt reflections.

However, illumination compensation enhances the migration artifacts. The scars produced by these problems are clearly visible in Figure 3. Due to its higher resolution, the 2.5D image seems even stronger affected than the 2D image.

*Experiment with scattering angle taper*

To reduce the migration artifacts, the next numerical experiment uses the weighted imaging condition (equation 11) with the scattering angle taper $\cos^3 \theta$ as the weight function. Figure 4 shows the results of 2D and 2.5D RTM, respectively.

While the differences between the 2D and 2.5D images are very much the same as commented on the previous set of figures, we see that the scattering angle taper has helped to improve both images, reducing the migration artifacts. The remaining artifacts are now affecting the two images in approximately the same way.
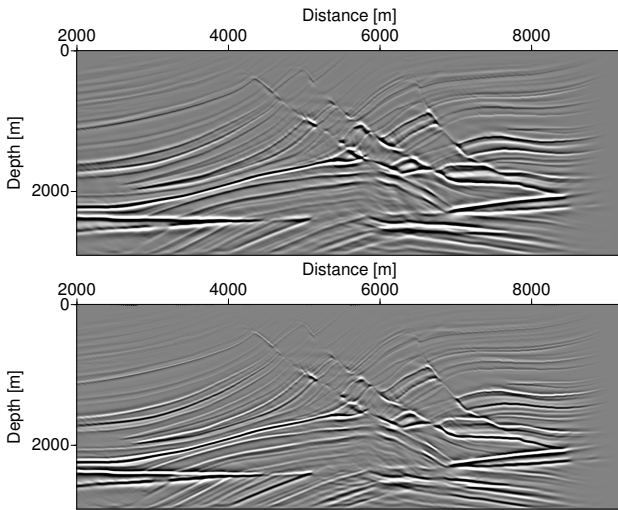
Figure 5: RTM images computed with scattering angle taper and obliquity correction in the weighted imaging condition (equation 11). Top: 2D image; bottom: 2.5D image.
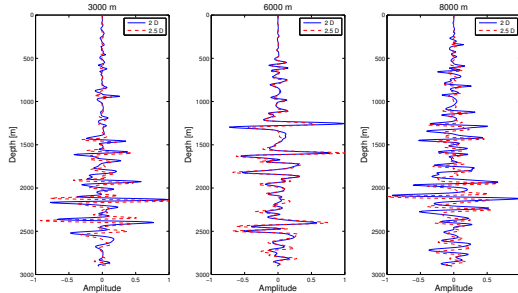


Figure 6: Comparison of 2D RTM (blue solid lines) and 2.5D RTM (red dashed lines) traces at $x = 3000$m, $x = 6000$m, and $x = 8000$m.
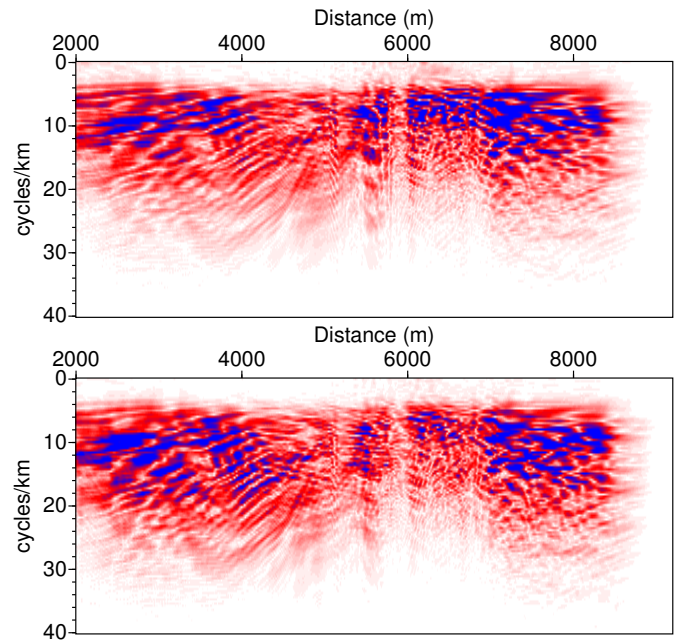


Figure 7: Wavenumber spectra of RTM images computed with scattering angle taper and obliquity correction in the weighted imaging condition (equation 11). Top: 2D image; bottom: 2.5D image.

*Experiment with obliquity correction*

Further improvement of the images can be achieved using the obliquity correction. The final numerical experiment uses the weighted image condition (equation 11) with the full weight function of equation 13, i.e., including both the scattering angle taper and the obliquity correction. Figure 5 shows the results of 2D and 2.5D RTM, respectively.

The obliquity compensation further reduces the backscattering artifacts. Moreover, it changes the amplitudes of different reflectors relative to each other. Again, its behavior on the 2D and 2.5D images is of the same nature. In both images, the backscattering artifacts are almost completely suppressed and, as a consequence, the image quality is visibly superior to that of the previous images. In this way, the 2.5D image takes full advantage of the higher resolution.

The effect of the 2.5D correction is even more evident in a trace-to-trace comparison. Figure 6 shows such a comparison for the traces of Figure 2 taken at $x = 3000$m, $x = 6000$m, and $x = 8000$m. The 2D RTM traces exhibit a stronger amplitude decay than the 2.5D RTM traces. The gain in resolution caused by the different pulse in 2D and 2.5D is most prominent in the deeper part of the image. Some events that are visible in the 2.5D traces have much lower amplitude or are even completely lost in the 2D traces.

While the improved imaging conditions using illumination compensation, scattering angle taper and obliquity correction reduce the amplitude discrepancies and the migration artifacts in the 2D and 2.5D images, the difference in resolution continues. This is clearly visible in all above images migrated with the two techniques. To make this point more evident, Figure 7 shows the wavenumber spectra of the images in Figure 5. We clearly observe the shift to higher wavenumber content at all central points. While the patterns of the spectra are comparable, the 2.5D spectrum has nonnegligible amplitudes up to higher wavenumbers. For instance, in the left part of the images, the strongest amplitudes (blue values) do not pass about 15 cycles/km in the 2D spectrum but reach about 20 cycles/km in the 2.5D spectrum. Intermediate amplitudes (dark red) in the 2D spectrum die out at about 20 cycles/km, while reaching about 25 cycles/km in the 2.5D spectrum. Only in the center region at about 6000 m, this effect is less pronounced.

In conclusion, our numerical experiments indicate that 2.5D RTM has a very beneficial effect on image quality, particularly in terms of its resolution. Moreover, when combined with illumination compensation, it also helps to improve amplitude recovery. Whenever these features are critical in an imaging project of 2D seismic data, the additional computational cost of 2.5D RTM over 2D RTM is justified.

## Conclusions

We implemented 2.5D RTM and evaluated our algorithm using the Marmousoft synthetic data set. The underlying 2.5D modelling algorithm consists of a sequence of independent 2D finite difference modelling steps in the mixed time-space/wavenumber domain. This characteristic makes the forward problem a truly parallel algorithm and its implementation very efficient in parallel architectures. In this way, the computational cost of 2.5D RTM is that of 2D RTM times the number of out-of-plane wavenumbers that need to be used, divided by the number of processing units available. The second and most important feature of 2.5D RTM is its low memory demand when compared to a 3D implementation, since only 2D snapshots needs to be stored during the process. The computational cost of the imaging conditions is identical in 2D or 2.5D and negligible compared to the cost of the wavefield extrapolation.

Our numerical experiments show the improved quality of 2.5D RTM images when compared to their 2D counterparts. The main advantage of 2.5D RTM is its higher resolution. This improves the delineation of subtle features in the image, as for example, faults and thin-layer boundaries. When combined with illumination compensation imaging conditions, our 2.5D RTM images also provided a clear improvement of amplitudes such that the resulting RTM amplitude variations were correlated to reflectivity changes. These improvements are sufficiently significant to justify the higher computational cost of 2.5D over 2D RTM whenever these features are critical to the success of an imaging project. Since 3D RTM generally has to be carried out on a coarse grid, the application of 2.5D RTM even may be advisable to produce high-resolution images of selected lines of a 3D survey.

### Acknowledgements

### References

Billette, F., S. L. Begat, P. Podvin, and G. Lambare, 2003, Practical aspects and applications of 2D stereotomography: Geophysics, **68**, 1008–1021.

Biondi, B., 2006, 3D seismic imaging: Society of Exploration Geophysicists.

Bleistein, N., 1986, Two-and-one-half dimensional in-plane wave propagation: Geophysical Prospecting, **34**, 686–703.

Chattopadhyay, S., and G. A. McMechan, 2008, Imaging conditions for prestack reverse-time migration: Geophysics, **73**, no. 3, S81–S89.

Chen, Y.-H., W. C. Chew, and M. L. Oristaglio, 1997, Application of perfectly matched layers to the transient modeling of subsurface problems: Geophysics, **62**, 1730–1736.

Claerbout, J., 1985, Imaging the earth's interior: Blackwell Scientific Publications.

Costa, J., A. Novais, F. S. Neto, and M. Tygel, 2005, 2.5D acoustic finite-difference modeling in variable density media: Journal of Seismic Exploration, **13**, 323–335.

Costa, J. C., F. A. S. Neto, M. R. M. Alcântara, J. Schleicher, and A. Novais, 2009, Obliquity-correction imaging condition for reverse time migration: Geophysics, **74**, S57–S66.

Haney, M. M., L. C. Bartel, D. F. Aldridge, and N. P. Symons, 2005, Insight into the output of reverse-time migration: What do amplitudes mean?: SEG International Annual Meeting, Expanded Abstracts, 1950–1953.

Harris, F. J., 1978, On the use of windows for harmonic analysis with the discrete Fourier transform: Proceedings of the IEEE, **66**, 51–83.

Kaelin, B., and A. Guitton, 2006, Imaging condition for reverse time migration: SEG International Annual Meeting, Expanded Abstracts, 2594–2597.

Liu, F., G. Zhang, S. A. Morton, and J. P. Leveille, 2011, An effective imaging condition for reverse-time migration using wavefield decomposition: Geophysics, **76**, S29–S39.

Novais, A., and L. Santos, 2005, 2.5D finite-difference solution of the acoustic wave equation: Geophysical Prospecting, **53**, 523–531.

Poole, T. L., A. Curtis, J. O. A. Robertsson, and D.-J. van Manen, 2010, Deconvolution imaging conditions and cross-talk suppression: Geophysics, **75**, W1–W12.

Schleicher, J., J. C. Costa, and A. Novais, 2008, A comparison of imaging conditions for wave-equation shot-profile migration: Geophysics, **73**, no. 6, S219–S227.

Valenciano, A., and B. Biondi, 2003, 2-D deconvolution imaging condition for shot-profile migration: SEG International Annual Meeting, Expanded Abstracts, 2431–2433.

Yoon, K., and K. Marfurt, 2006, Reverse-time migration using the Poynting vector: Exploration Geophysics, **37**, 102–107.